Noname manuscript No.
(will be inserted by the editor)

Heterogeneous nocturnal cooling in a large basin under very stable conditions

D. Martínez · M. A. Jiménez · J. Cuxart · L. Mahrt

Received: date / Accepted: date

Abstract Large basins with relatively wide floors experience heterogeneous nocturnal cooling due to the diversity of the topography and the land use within the basin. Near the mountain ranges the drainage flows prevail, but in the low areas, river valleys or embedded plateaux, the actual rates of cooling differ as does the behaviour of the local flows in the first few meters above the surface. In this study, the temporal and spatial heterogeneity of the surface cooling is inspected through the analysis of satellite radiative surface temperature, data from a meteorological network and a tall tower. The organisation of the flow within the basin is also studied by means of a high-resolution mesoscale simulation. Although the basin cools almost as a unit, there exists a large diversity of local regimes. Vertical profiles from the mesoscale simulation are analysed and grouped according to their wind structure and stratification.

Keywords Basin flows · Mesoscale modelling · Satellite images · Stable boundary layer · Surface heterogeneity

1 Introduction

Large river basins that are topographically confined have distinct local meteorological characteristics. A well defined synoptic flow can cause specific patterns within the basin. Furthermore, heated upslope/upvalley daytime flows

D. Martínez · M. A. Jiménez · J. Cuxart · L. Mahrt
Grup de Meteorologia, Dpt. Física, Univ. de les Illes Balears
Cra. Valldemossa, km. 7.5, 07122 - Palma, Mallorca (Illes Balears)
Tel.: +34-971-172506
E-mail: dani.martinez@uib.cat

L. Mahrt *on leave from*
College of Oceanic and Atmospheric Science
Oregon State University, Corvallis, Oregon 97331
Tel.: (541) 737-5691
E-mail: mahrt@coas.oregonstate.edu

and nocturnal downslope/downvalley flows near the surface can co-exist with the general flow. Slope flows can be eliminated if the general flow is strong or the skies are overcast, but can predominate if the synoptic wind is weak and the skies are clear. Terrain heterogeneity generates patterns of temperature and circulation that are particular to each basin, having nocturnal drainage flows from the mountain ranges and surrounding gentle slopes towards the centre of the basin, and cold air pooling in local depressions or specific dynamics over elevated plateaux. The local thermal and wind profiles are therefore very different between these areas at night.

Some studies for large basins have reported several defining characteristics. Studies made for the USA intermountain western basin (Wolyn and McKee 1989; Whiteman et al. 1999; Zhong et al. 2001) show that the air within the basin can be stably stratified from bottom to top (more than 1000 m of depth) for several days if warm advection aloft prevails. Near the ground, a diurnal cycle is observed, with inversions stronger than 10 K over several hundred metres depth during the night and neutrality or convection depending on the solar forcing and the situation aloft during the day. Zhong et al. (2004) inspect the wind and thermal patterns within the California's Central valley, driven by a mesoscale thermal forcing, due to the land-ocean thermal contrasts under fair weather conditions. The subsequent formation of a low-level jet at night interacts with the local-scale slope flows along the foothills. The sensitivity of the simulated low-level winds to the soil initialisation and large-scale atmospheric patterns are analysed in Michelson and Bao (2008).

The dynamics of quasi-ideal cold pools have been studied for small structures, using observations as at Peter Sinks (Utah, Clements et al. 2003) or in elevated alpine basins (Zängl 2005a and 2005b). Clements et al. (2003) show that drainage flows are relevant in the first part of the night on the 1-km scale Peter Sinks basin, contributing to the initial pooling, but they disappeared after the formation of the cold pool, which continued to intensify. Vosper and Brown (2008) study topographically induced cold pools with a two-dimensional (2D) numerical model and demonstrate that the results are very dependent on the wind velocity above the depression and sensitive to cloudiness. In order to locate the areas of the landscape that are likely to be prone to cold-air pooling, Lundquist et al. (2008) developed an algorithm based on the local characteristics of the terrain.

The interaction of drainage flows and cold pools is inspected in Neff and King (1989) for a basin of intermediate size (De Beque, Colorado, USA, of 30 km of radius), where the cold pool is formed and can extend to an open area outside the basin. The tributary valleys have drainage flows down their axes, which then often flow over the cold pool air above the valley floor. Sometimes the drainage flow is colder than the air in the cold pool and penetrates underneath. A similar pattern was found by Cuxart et al. (2007) for a numerical study of the Palma Basin on Majorca Island, which is of comparable dimension (20 km of radius). There, the drainage flow coming from the Randa Mountain was circulating over the cold pool except the very cold and thin skin flow that penetrated under the pool.

The current work seeks to understand the behaviour of the stably stratified boundary layer (SBL) within a wide basin. The Duero basin, in the north-west part of the Iberian Peninsula, covers 97290 km^2 of which 78952 km^2 are in the Spanish part (160 km of radius), a sub area that is basically a closed basin connected to the Portugal part of the basin by a narrow pass. The airflow has been extensively studied during the last decade, using data from SABLES-98 (Cuxart et al. 2000a) and data gathered afterwards (Conangla et al. 2008; Viana et al. 2009) over an elevated plateau at the central part of the basin where the Research Centre for the Lower Atmosphere (CIBA) is located with a 100 m tower (Figure 1). The statistics of the wind data gathered at this site (Conangla and Cuxart 2006) show that there must be a mesoscale forcing to explain the behaviour of the direction of the wind. Cuxart (2008), aided by the mesoscale simulations of Bravo et al. (2008), proposes a nocturnal basin-scale organisation to explain the data. The details of a well defined katabatic flow over the southern mountain range were analysed in Martínez and Cuxart (2009).

The main objective of this work is to study the behaviour of the basin-scale airflow close to the ground during nighttime conditions. A case study for a very stable night (14 to 15 January 2003) is explored using different available observations, described in section 2. This night belongs to a ten-month period when the instruments on the CIBA tower functioned perfectly following calibration. The period has been analysed statistically (Conangla et al. 2008) and the case selected for this study has been previously modelled in Bravo et al. (2008). A description of the night is shown in section 3. The observed patterns are analysed using satellite imagery, which illustrate the within-basin heterogeneity, and compared with results from a high-resolution mesoscale simulation, shown in section 4. The within-basin heterogeneity of the near-the-surface air from the mesoscale simulation is inspected in section 5, where the geographical distribution of the different features is analysed. Conclusions are presented in section 6.

2 Tools

This study uses the network of Automatic Weather Stations (AWS) of the Spanish Meteorological Service (AEMET), the NOAA and METEOSAT imagery and data from the CIBA site. In addition a high-resolution mesoscale simulation is verified against the observational information.

Satellite imagery: Meteosat-7 derived surface radiative temperatures are used (Prata et al. 1995), one every 30 minutes with a spatial resolution of about 25 km^2 per pixel in the area of interest. These images are corrected except for the removal of the water vapour effect, which implies that estimated values are 1 to 2 K colder than with the full correction (Coll et al. 1994). On the nights with frost formation, as in the present case, the surface emissivity may vary overnight leading to additional errors in the radiative temperature structure.

A NOAA image corresponding to 0200 UTC for the area is also used, that provides finer spatial resolution (about 1 km^2) which includes geometrical, navigation and water vapour corrections, as in Coll and Caselles (1997). The uses of these images are similar to what is done in Jiménez et al. (2008).

19 Automatic weather stations: The weather stations are irregularly distributed throughout the basin (Figure 1). They measure wind speed and direction at 10 m above ground level (a.g.l.) and temperature and humidity at 1.5 m a.g.l. We include 1 record every hour. For this very stable night with extremely weak winds, the wind sensors are often not working because their threshold is higher than 0.5 m s^{-1}.

CIBA 100-m mast: Provided with four Metek sonic anemometers with a sampling rate of 20 Hz (at levels 96.6 m, 49.6 m, 19.6 m, 5.6 m), 5 cup anemometers made by Risoe National laboratory of Denmark with a threshold of 0.5 m s^{-1} (at levels 98.6 m, 74.6 m, 34.6 m, 9.6 m, 2.2 m) sampled 5 times per second; slow temperature sensors at 97.5 m, 35.5 m, 20.5 m, 10.5 m, 2.3 m and humidity sensors at 97 m, and 10 m. 5-min averaged data and turbulence statistics are stored routinely.

Mesoscale simulation: The Meso-NH model (Lafore et al. 1998) is run using a single domain (640 x 500 km^2) with 2 km of horizontal resolution, and a very fine vertical resolution of 3 m near the surface, degrading gradually with height (for instance, a resolution of 5 m at 100 m a.g.l.). This configuration captures the main topographical features within the basin, allowing the dynamics to represent the advective motions generated and conditioned by the topography. The numerical simulation begins at noon 14 January and extends for 24 hours, initialised using an analysis of the European Centre for Medium-Range Weather Forecasts (ECMWF), refreshing the lateral boundary conditions every 6 h. Since the synoptic forcing is very weak for this case, the physics of the model and the soil heterogeneity play a central role. These include the 1.5 order turbulence scheme (Cuxart et al. 2000b), the Morcrette radiation scheme (Morcrette 1990) and the Interaction Soil Biosphere Atmosphere (ISBA) soil-vegetation schema (Noilhan and Planton 1989). Since no clouds or fog were observed during the night, the numerical simulation is made without the activation of the condensation scheme, although the surface scheme accounts for these condensation processes in the surface energy budget. The soil conditions are initialised using information from the ECMWF and the soil heterogeneity comes from the CORINE data base (Heymann et al. 1994). The water content from the ECMWF is integrated into the model in a way that prevents any water imbalance (Le Moigne, personal communication). The same setup is described for another location in Jiménez et al. (2008).

3 Description of the night

The combined use of all the available observational information and of the mesoscale simulation provides a good picture of the atmosphere dynamics within the basin. The basin (taken here as the almost closed Spanish part of the Duero basin) has its bottom near 750 m above sea level (a.s.l.) and it is surrounded by mountain ranges peaking at 2500 m a.s.l. except for lower topography at the western edge (Figure 1a). The bottom part has some minor heterogeneities, such as elevated plateaux between the river valleys (height differences of about 100 m between plateau and river valley). The Pisuerga tributary is oriented from north-east to south-west and meets the Duero river (that runs primarily east-west) close to Valladolid (location x09 in the plots).

The centre of the high pressure system is approximately over the basin, characterising the area with clear skies and a weak synoptic flow that lead to strong nocturnal cooling. The night-averaged value of the stability parameter z/L calculated from data at the CIBA site is 2.5, where L is the Obukhov length and z is the height above the ground (5.6 m in this case). According to Figure 1 in Mahrt et al. (1998), the stability parameter (z/L) corresponds to very stable conditions, as in the night analysed in Conangla et al. (2008). Their study found that 14% of the nocturnal periods at the CIBA site belonged to the very stable category.

The mesoscale simulation shows that this day is characterised by within-basin circulations that, at night, include drainage flows from the mountain ranges to the centre of the basin with wind maxima at heights of about 30 to 60 m a.g.l. These flows have longitudinal scales of several tens of km to about 100 km, that are diverted by the local topography and can interact when they meet (see Figure 1a). They have different origins and only a small percentage can be classified as katabatic flows. Under very stable conditions, the likely presence of gravity waves (Terradellas et al. 2001) is restricted in the mesoscale simulation to those with a wavelength of the same order of the horizontal resolution.

Close to the ground, the very local terrain heterogeneities largely determine the variation of the meteorological variables, as illustrated by the satellite derived radiative surface temperatures and the observed and modelled 1.5-m temperatures (see Figure 1b for the later case). The differences in the minimum temperature between AWS are smaller than 4 K and the winds are very weak, usually below the threshold of the anemometers. In general the measurements near the ground seem to be disconnected from the stronger winds aloft, except in the areas where well formed katabatic winds prevail. Air on the elevated plateaux and in cold pools or river valleys can be calm and cold. Their characteristics will be discussed in the following sections.

To assess the model accuracy, results are compared to the CIBA values as shown in Figure 2. The observed wind at the beginning of the night veers at a faster rate (double) than an inertial oscillation -which is the behaviour of the model- as reported for other cases (Cuxart 2008). This difference may be related to factors like thermal basin heterogeneity at the end of the daytime

not well captured by the model. In the second part of the night (after 2200 UTC), a low-level jet is established below 100 m a.g.l. and the model compares more closely to the data, although the wind speed is slightly underestimated at the upper levels of the tower because the simulation does not capture properly the shape of the low-level jet.

The temperature between 10 and 100 m a.g.l. is well reproduced at the CIBA site, being almost stationary at 100 m a.g.l. (940 m a.s.l.) during the night. Therefore, the difference between the 1.5-m temperature for the AWS and the 100-m temperature is a measure of the strength of the temperature inversion for different parts of the basin (Figure 3). The Turbulence Kinetic Energy (TKE) is relatively weak in the daytime, corresponding to a very shallow winter convective boundary layer and the observed values at nighttime are very small and near zero in the model. The increase of the differences between the model and the observations through the night leads to simulated convection that is shallower and weaker than the observed convection the next morning. In the model, the increase in the TKE is delayed approximately 2 hours at 10 m a.g.l. and is non-existent at 100 m a.g.l. Figure 3 shows that the evolution of the CIBA and the AWS temperature at 1.5 m a.g.l. differ from the model, with differences that are not systematic, some places being colder and vice versa. At the points where the simulation generates a jet, the mixing of the air close to the surface leads to a smaller cooling than the observations (not shown). This is the case for the grid point in the cold pool (x12) and in the river valley (x09). In contrast, at the CIBA site, the 1.5-m temperature fall is larger in the simulation due to the lack of turbulence generated in the model for this point. For that night, many observation locations reported the formation of frost. Therefore, the latent heat released by the frost formation may reduce the temperature decrease close to the surface (Whiteman et al. 2007).

Summarising, the model is able to generate a system of low-level flows organised at the basin scale, with katabatic winds on the gentle slopes between the mountain ranges and in the Duero river central valley. The model has a level of heterogeneity similar to what the observations show, but not precisely at the same locations. The evolution of the wind direction is well captured in the CIBA site after 2200 UTC but missing an earlier fast veering, probably because of incomplete representation of the previous afternoon basin dynamics in the model. A quantitative estimation of the heterogeneity of the basin, as seen by the satellite images, the AWS and the model, is presented in the next section.

4 Spatial distribution and time evolution of surface temperature

To analyse the spatial variability and the temporal evolution of the temperature near the surface, we use half-hourly values of radiative surface temperature for the complete basin, estimated from the Meteosat-7 images, and use hourly values of the 1.5-m temperature as measured by the AWS network.

Temperature at the surface and the 1.5-m level will also be analysed from the mesoscale simulation.

The two temperature fields are not directly comparable, especially in very stable conditions when large temperature gradients can exist in the first few meters above the ground and the surface energy budget depends strongly on the state of the surface (Jiménez et al. 2008). Surface temperature will mostly reflect the local energy budget in the layer adjacent to the ground, whereas the 1.5-m temperature may be influenced by larger scale atmospheric transport. Strong stratification near the ground may restrict exchange of heat between the 1.5-m level and the surface.

The time-space variation of both temperatures are examined using a decomposition similar to that in Lundquist et al. (2008):

$$T_b(\mathbf{x},t) = \overline{T}_b(\mathbf{x}) + \overline{\overline{T}}_b(t) + \widetilde{T}_b(\mathbf{x},t) \tag{1}$$

where the brightness surface temperature $T_b(\mathbf{x},t)$ is split into three terms,

(i) the mean nocturnal temperature $\overline{T}_b(\mathbf{x})$ is based on averaging all available values for each pixel or gridbox during the night (1730-0730 UTC), thus providing the average surface temperature pattern (this is a single 2D-field for the entire night). The spatial average of $\overline{T}_b(\mathbf{x})$ defines the mean nocturnal temperature;

(ii) the basin-averaged deviation of the temperature from the mean nocturnal temperature $\overline{\overline{T}}_b(t)$ reflects the general cooling of the basin during the night (this is a time series of one value for the whole basin);

(iii) the local spatial deviation $\widetilde{T}_b(\mathbf{x},t)$ represents the additional information that is not explained by the previous two terms (it is a 2D-field).

The brightness surface temperature is analysed from the data provided by Meteosat-7 images and from the mesoscale simulation. The NOAA image at 0200 UTC with higher resolution provides similar patterns as Meteosat-7 for that hour. All the images are corrected, but Meteosat-7 provides a field that does not subtract the effect of water vapour and has a bias of about 1.5 K colder than the NOAA temperatures, for which this correction is performed. Since the model does not use a snow pack parameterisation, the simulation predicts different surface temperatures compared to the satellite observations for the snow-covered part of the south-western basin. The decomposition of the radiative surface temperature from the satellite data does not change significantly when the snow-covered areas are considered.

Mean nocturnal temperature, $\overline{T}_b(\mathbf{x})$: The nocturnal average $\overline{T}_b(\mathbf{x})$ for the basin (Figure 4a) computed from the satellite images shows the colder areas in blue. These areas are found over the mountain ranges and in certain parts of the centre of the basin, namely a small cold pool (x12), an area in the river valley (x09) and some locations on the elevated plateaux (such as the CIBA site). Warmer parts include the northern part of the basin and the south-east

of x12, where well defined katabatic flows persist and can be detected as a warmer signal in the satellite images (Bromwich 1989).

The mesoscale simulation, that does not well capture the snow covered area in the south-west, shows absolute average values of about 1 K warmer than the satellite temperature (not shown), which is in the range of the error caused by the non-removal of the water vapour effect, as the NOAA image for 0200 UTC seems to confirm. The simulation also generates the coldest areas over the elevated plateaux and, to a lesser degree, in the cold pools east of x12 and x18. The total spatial variability is of the same order, about 4 K, in both fields.

Basin-averaged deviation, $\overline{\overline{T}}_b(t)$: Figure 5a shows that the evolution of the averaged basin deviation from the mean nocturnal surface temperature can be fit to a quadratic function:

$$\overline{\overline{T}}_b(t) = At^2 + Bt + C \tag{2}$$

where t represents the time in seconds after the sunset. The linear term is an order of magnitude larger than the quadratic term. It is obvious that the model experiences a much larger surface temperature decrease during the night (about 7 K) than the temperature decrease observed by the satellite (about 3.5 K). Part of the difference comes from the different horizontal resolution of the fields, coarser for the satellite (Jiménez el al. 2008), and from the formation of frost within the basin. The accumulation of frost on the ground increases the surface emissivity during the night, leading to an observed fall of the radiative surface temperature on the order of 1 K smaller than the actual one. Another possibility is an inadequate representation of the surface energy budget in the model, which is forced to close point by point (the ground heat flux must equal the sum of the other fluxes and the land surface temperature is the temperature that fulfils this requirement). The observed energy balance can have large departures from the closure that are suspected to come from the inadequacy of measurements or from the local inhomogeneities. Finally, biases in the soil moisture derived from the original ECMWF fields could also have an effect on the surface temperature and moisture provided by the soil scheme, leading to an error in the representation of the ground heat flux.

In both cases, the cooling is faster in the first part of the night compared to the second part, indicating that a better fit is obtained through a quadratic adjustment. Whiteman et al. (2004) also found that the decrease of the surface temperature was faster during the first part of the night, represented in their cases by an exponential function. They suggest that, under windless conditions, the longwave cooling of the surface is counteracted by the downward longwave radiation and the ground heat flux. As the surface temperature decreases with time, the net longwave radiation is asymptotically balanced by the ground heat flux, leading to a smaller cooling of the surface during the second part of the night.

When the same curves are produced with the model 1.5-m temperature and the network of AWS (Figure 5b), the model temperature decreases about

6 K and the observations decrease 5.5 K. This indicates that the model has similar cooling for the surface and 1.5-m levels. For the observations, after the rapid surface cooling just before sunset (not shown), the temperature decrease at the 1.5-m level exceeds the surface cooling, indicating that there may be issues still to address in the treatment of the image surface temperature.

Local spatial deviation, $\widetilde{T}_b(\mathbf{x}, t)$: The last term of Equation 1 is shown in Figure 4b, which reveals the areas that have been cooled more than 4 K between 1730 (beginning of the night) and 0730 UTC. This threshold represents a surface nocturnal cooling 0.5 K greater than the mean cooling of the basin, showing the area where the absolute cooling with respect to the temperature at sunset has been stronger. The large cooling occupies an area at the centre of the basin, covering the elevated plateaux (the CIBA site and x24), the Duero and Pisuerga valleys (x09) and the cold pool close to station x12. Another cold area in the western part of the basin is found around station x18. The mesoscale simulation shows a pattern of the surface nocturnal cooling more constrained by the topography (not shown), with spatial detail that cannot be achieved by the satellite imagery. However, the areas with a larger total cooling include those revealed by Figure 4b. This figure illustrates the heterogeneity of the surface cooling within a large basin. Some of the features for the different kind of areas will be studied in the next section by means of the mesoscale simulation.

5 Simulated within-basin flow heterogeneities

To inspect the heterogeneity of the wind and temperature fields in the area of interest, each column of the model outputs for 0000 UTC within the domain (Figure 1) has been analysed. Although there are significant differences between the simulation and observations, it is not possible to account for the within-basin flow heteregeneity of the meteorological variables with the available experimental data. The wind speed in the first 100 m a.g.l. has been examined to determine if there is a jet, defined as a maximum in the wind speed in this layer with a decrease in speed of at least 0.5 m s^{-1} above the height of the maximum. The analysis is restricted to the first 100 m because the wind maximum within the basin usually appears at heights between 30 to 60 m a.g.l. The strength of stratification near the ground has been estimated using the difference of potential temperatures between the levels at 10.5 and 1.5 m a.g.l., corresponding to the fourth and the first vertical levels of the simulation.

In Table 1, data is arbitrarily classified according to five categories for the wind and four categories for the stratification. The first three lines correspond to weak, moderate and strong jets, respectively, and the two last lines to grid points without a jet in the first 100 m a.g.l. The first column corresponds to unstable stratification, and the other three to sequentially increasing stable

stratification. Every grid point is included into one of the resulting 20 categories.

Figure 6a describes the five wind categories for the selected area and Figure 6b describes the three stably stratified ones. Half of the points have a jet in the first 100 m a.g.l., almost all of them being weak ($u_{max} \leq 2$ m s^{-1}) or moderate ($2 < u_{max} \leq 4$ m s^{-1}). The strong ones ($u_{max} > 4$ m s^{-1}) represent only a 2.4% of the total. The points without a jet have been separated into weak ($u_{max} < 2$ m s^{-1}) and moderate ($u_{max} \geq 2$ m s^{-1}) winds.

The strong jets occur for only a few selected areas within the basin that have significantly larger local slope, the blue area at the south-east part of Figure 6a representing a well-defined downslope flow that has already been analysed in Martínez and Cuxart (2009). The moderate jets (green) occupy one-fourth of the analysed area, mostly on the slopes of the mountain ranges to the south and south-east of the basin. In contrast, the northern part of the basin with smaller regional slope, is mostly covered by weak jets (red) or weak winds (yellow). Most of the weak winds with no jet tend to be found over the river valleys and some over the elevated plateaux. The points without jets and the wind speed above 2 m s^{-1} in the first 100 m a.g.l. (non coloured points in Figure 6a) are found basically at the higher mountain locations and outside the basin, and we will not consider them further.

Figure 6b plots the three stably stratified categories, after excluding the non-jet moderate cases. We also exclude the unstable cases, amounting to only 0.26% of the total area. Most of the area is covered by weakly stratified surface layers (in red), located in the foothills and also in the river valleys. The moderately stratified points are found mostly at the centre of the basin (green), whereas the plateaux contain the strongest stratification (blue). About 80% of the points with a jet have weakly stratified surface layers and only 2% have strong stratification, basically with weak jets. In contrast, the no-jet weak wind cases have more occurrences of moderate and strong surface layer stratification (about 50%).

The average profiles of wind and temperature for the categories in Table 1 are shown in Figures 7a and 7b, respectively. Each wind profile is made by averaging all the occurrences of stably stratified categories (one profile for each of the first four lines in the Table 1). Figure 7a shows that, on average, the level of maximum speed above the surface increases as the jet strengthens. The standard deviations (not shown) for the three jet categories do not overlap. This statistical relationship is not described by any simple analytical model, like the Prandtl model for katabatic flows (Grisogono and Oerlemans 2001). The jets that contribute to the average profiles have different origins and, as a result, these jets are unlikely to be described by such simple models. The stronger jets, which amount to only 2.4% of the total of the area, have an average value of 4.6 m s^{-1} above 40 m a.g.l. Within the basin, the weak jets, moderate jets, and weak wind no-jet cases each occupy about 1/3 of the area, the moderate ones with the jet maximum at about 25 m a.g.l. over the south-east, and the weak jet and no-jet points co-existing over the rest of the basin with very similar values of the wind speed and surface layer stratification.

The points with different surface layer stable stratification are drawn in Figure 7b, corresponding to the averages of columns 3, 4 and 5 of Table 1. The no-jet moderate winds, which lie outside the basin interior, are excluded. The weakly stratified case includes most of the jet points and about half of the weak non-jet points. It is seen that this average shows a weakly stable layer extending up to 25 m a.g.l. and a gradual transition to the upper levels. In contrast, the moderately and strongly stratified cases have a strong surface based inversion of about 10 to 15 m a.g.l. (of 3 K and 4.5 K respectively) and a sharp transition above.

The relative contribution of the radiative and turbulent terms to the temperature evolution is shown in Figure 8 for the profiles of Figure 7b, without considering the advection and latent heat flux terms. Figure 8 is given in a logarithmic scale for height to emphasise the characteristics near the surface. The vertical divergence of the net radiation (Figure 8a) cools all the column with very similar integrated values for all the cases and -0.0004 K s^{-1} near the surface regardless of the stratification. The strongly stratified case (in 3.32% of the area, mostly with weak wind jet and no-jet cases) shows a layer of warming between the first and second atmospheric layers of the model, similarly to what Savijärvi (2006) and Edwards (2009) report for SBLs with weak winds close to the ground.

The vertical divergence of the turbulence flux shows large differences between the regimes, but they all are the dominant cooling mechanism in the surface layer and also warm the air closest to the surface, as in Gopalakrishnan et al. (1998). The turbulent heat flux convergence warms the air below 3 m for the weakly stratified cases and can exceed the effect of the surface radiative cooling. The average heat flux divergence for the moderately stratified case corresponds to warming only near the ground and is in equilibrium there with the radiation cooling. For the average strongly stratified case, the maximum of TKE occurs just above the layer of radiative warming.

6 Conclusions

This study, based on a tall tower, surface meteorological network and satellite data and a mesoscale simulation, documents the large variability of nocturnal cooling within a large basin. The basin includes an isolated modest plateau near the centre, plus gentle slopes (angles of 0.003 rad) converging to the centre from the northern and southern mountain ranges.

The analysis of the evolution of the radiative surface temperature fields obtained from Meteosat-7 allows the characterisation of the terrain heterogeneity. The basin area-averaged surface temperature based on satellite data cools about 3.5 K between sunset and sunrise, with large within-basin variability. The surface temperature decrease during the same time-period is double in the simulation (7 K). This difference is partially explained by the formation of frost during the night, since its effect increases the surface emissivity and leads to a satellite estimate smaller than the actual surface cooling. At 1.5-m height,

the AWS network and the model provide similar nocturnal cooling, close to 6 K. The similar decrease of the temperature at the surface and at 1.5 m a.g.l. in the simulation, at the basin scale, indicates that the model efficiently couples the surface and the first computation level. The areas where drainage flows prevail, turbulent mixing of the air close to the ground leads to less cooling compared to more stagnant areas. A time-space decomposition of the temperature field documents the time dependence of the coldest and warmest areas. It is important to note that cold air also collects on the elevated plateau in the centre of the basin, which is colder than the basin-averaged temperature.

The mesoscale simulation is not able to reproduce exactly the spatial distribution of warm and cold areas, although the amount of heterogeneity in the basin is well captured. The model results were used to explore the within-basin variability. More than half of the columns have a wind jet in the lowest 100 m, usually with a maximum speed between 1 and 4 m s^{-1} and located below the 45-m level. The moderate jets dominate the airflow over the foothills and the weak jets dominate over gentle slopes, with no-jet weak winds occurring along the river valleys and over the plateaux. These jets have different origins and only a small percentage can be classified as katabatic flows and, therefore, cannot be analysed with the simple analytical models available in the literature. For the cases with jets, the stratification is weakly stable and the turbulence is the dominant cooling mechanism. For the strongly stratified cases near the surface, the turbulence flux convergence tends to warm partially the air and compensate for the effect of surface radiative cooling. Measurement of such turbulent flux convergence would require high quality flux measurements with fine vertical resolution.

Acknowledgements ECMWF and AEMET are thanked for the access to computing time, AEMET also for the data from the AWS network, University of Valladolid for the CIBA data, EUMETSAT and NOAA for the satellite images, and the Meso-NH team in Meteo France and Laboratoire d'Aérologie for the technical support and maintenance of the modelling system. The University of the Balearic Islands (UIB) is thanked for providing the financial support for the visit of Dr. Mahrt to the Department of Meteorology at the UIB. This work was partially funded through grants CGL2006-12474-C03, CGL2009-12797-C03 and BES-2007-16272 of the Spanish Government which include European Regional funds (FEDER). The authors are indebted to the three reviewers, who have helped to improve the manuscript substantially.

REFERENCES

Bravo M, Mira A, Soler MR, Cuxart J (2008) Intercomparison and evaluation of MM5 and Meso-NH mesoscale models in the stable boundary layer. Boundary-Layer Meteorol 128:77-101

Bromwich DH (1989) Satellite Analyses of antarctic katabatic wind behavior. Bull Am Meteorol Soc 70:738-749

Clements CB, Whiteman CD, Horel JD (2003) Cold-air-pool structure and evolution in a mountain basin: Peter Sinks, Utah. J Appl Meteorol 42:752-768

Coll C, Caselles V, Sobrino JA, Valor E (1994) On the atmospheric dependence of the split-window equation for land surface temperature. Int J Rem Sens 15:105-122

Coll C, Caselles V (1997) A split-window algorithm for land surface temperature from advanced very high resolution radiometer data: Validation and algorithm comparison. J Geophys Res 102:697-713

Conangla L, Cuxart J (2006) On the turbulence in the upper part of the low-level jet: an experimental and numerical study. Boundary-Layer Meteorol 118:379-400

Conangla L, Cuxart J, Soler MR (2008) Characterisation of the nocturnal boundary layer at a site in northern Spain. Boundary-Layer Meteorol 128:255-276

Cuxart J, Yagüe C, Morales G, Terradellas E, Orbe J, Calvo J, Fernandez A, Soler MR, Infante C, Buenestado P, Espinalt A, Joergensen HE, Rees JM, Vilá J, Redondo JM, Cantalapiedra IR, Conangla L (2000a) Stable Atmospheric Boundary-Layer Experiment in Spain (SABLES 98): A report. Boundary-Layer Meteorol 96:337-370

Cuxart J, Bougeault P, Redelsperger J-L (2000b) A turbulence scheme allowing for mesoscale and large-eddy simulations. Q J Roy Meteorol Soc 126:1-30

Cuxart J, Jiménez MA, Martínez D (2007) Nocturnal mesobeta basin and katabatic flows on a midlatitude island. Mon Weather Rev 135:918-932

Cuxart J (2008) Nocturnal basin low-level jets: an integrated study. Acta Geophys Pol 56:100-113

Edwards JM (2009) Radiative processes in the stable boundary layer: part II. The development of the nocturnal boundary layer. Boundary-Layer Meteorol 131:127-146

Gopalakrishnan SG, Maithili Sharan, McNider RT, Singh MP (1998) Study of radiative and turbulent processes in the stable boundary layer under weak wind conditions. J Atmos Sci 55:954-960

Grisogono B, Oerlemans J (2001) Katabatic flow: analytic solution for gradually varying eddy diffusivities. J Atmos Sci 58:3349-3354

Heymann Y, Steenmans C, Croissille G, Bossard M (1994) Corine land cover technical guide. Office for official publications of the European communities, Luxembourg, 136 pp.

Jiménez MA, Mira A, Cuxart J, Luque A, Alonso S, Guijarro JA (2008) Verification of a clear-sky mesoscale simulation using satellite-derived surface temperatures. Mon Weather Rev 136:5148-5161

Lafore JP, Stein J, Asencio N, Bougeault P, Ducrocq V, Duron J, Fisher C, Héreil P, Mascart P, Pinty JP, Redelsperger J-L, Richard E, Vilá-Guerau de Arellano J (1998) The Meso-NH atmospheric simulation system. Part I: Adiabatic formulation and control simulation. Ann Geophys 16:90-109

Lundquist JD, Pepin N, Rochford C (2008) Automated algorithm for mapping regions of cold-air pooling in complex terrain. J Geophys Res 113:D22107-1-15

Mahrt L, Sun J, Blumen W, Delany T, Oncley S (1998) Nocturnal boundary-layer regimes. Boundary-Layer Meteorol 88:255-278

Martínez D, Cuxart J (2009) Assesment of the hydraulic slope flow approach using a mesoscale model. Acta Geophys Pol 57:882-903

Michelson SA, Bao JW (2008) Sensitivity of low-level winds simulated by the WRF model in California's Central valley to uncertainties in the large-scale forcing and soil initialization. J Appl Meteorol Clim 47:3131-3149

Morcrette J-J (1990) Impact of changes to the radiation transfer parameterizations plus cloud optical properties in the ECMWF model. Mon Weather Rev 118:847-873

Neff WD, King CW (1989) The accumulation and pooling of drainage flows in a large basin. J Appl Meteorol 28:518-529

Noilhan J, Planton S (1989) A simple parameterization of land surface processes for meteorological models. Mon Weather Rev 117:536-549

Prata AJ, Caselles V, Coll C, Sobrino JA, Otllé C (1995) Thermal remote sensing of land surface temperature from satellites: current status and future prospects. Rem Sens Environ 12:175-224

Savijärvi H (2006) Radiative and turbulent heating rates in the clear-air boundary layer. Q J Roy Meteorol Soc 132:147-161

Terradellas E, Morales G, Cuxart J, Yagüe C (2001) Wavelet methods: application to the study of the stable atmospheric boundary layer under non-stationary conditions. Dyn Atmos Oceans 34:225-244

Viana S, Yagüe C, Maqueda G (2009) Propagation and effects of a mesoscale gravity wave over a weakly-stratified nocturnal boundary layer during the SABLES2006 field campaign. Boundary-Layer Meteorol 133:165-188

Vosper SB, Brown AR (2008) Numerical simulations of sheltering in valleys: the formation of nighttime cold-air pools. Boundary-Layer Meteorol 127:429-448

Whiteman CD, Bian X, Zhong S (1999) Wintertime evolution of the temperature inversion in the Colorado plateau basin. J Appl Meteorol 38:1103-1117

Whiteman CD, Haiden T, Pospichal B, Eisenbach S, Steinacker R (2004) Minimum temperatures, diurnal temperature ranges, and temperature inversions in limestone sinkholes of different sizes and shapes. J Appl Meteorol 43:1224-1236

Whiteman CD, De Wekker SFL, Haiden T (2007) Effect of dewfall and frostfall on nighttime cooling in a small, closed basin. J Appl Meteorol Clim 46:3-13

Wolyn PG, McKee TB (1989) Deep stable layers in the intermountain western United States. Mon Weather Rev 117:461-472

Zängl G (2005a) Formation of extreme cold-air pools in elevated sinkholes: an idealized numerical process study. Mon Weather Rev 133:925-941

Zängl G (2005b) Dynamical aspects of wintertime cold-air pools in an alpine valley system. Mon Weather Rev 133:2721-2740

Zhong S, Whiteman CD, Bian X, Shaw WJ, Hubble JM (2001) Meteorological processes affecting the evolution of a wintertime cold air pool in the Columbia basin. Mon Weather Rev 129:2600-2613

Zhong S, Whiteman CD, Bian X (2004) Diurnal evolution of three-dimensional wind and temperature structure in California's Central valley. J Appl Meteorol 43:1679-1699

Table 1 Percentage of the cases (19430 in total) for the classification of the points at 0000 UTC according to the wind maxima (up to 100 m) and the temperature gradient (up to 10 m where $\Delta\theta = \theta_{10.5m} - \theta_{1.5m}$). The jet category requires that the wind above the jet is, at least, 0.5 m s^{-1} smaller than in the jet height.

	$\Delta\theta < 0$ K	$0 \leq \Delta\theta < 2$ K	$2 \leq \Delta\theta < 4$ K	$\Delta\theta \geq 4$ K	Total
weak jet ($0.5 < wind_{max} \leq 2$ m s^{-1})	0.04	18.08	6.85	1.02	**25.99**
moderate jet ($2 < wind_{max} \leq 4$ m s^{-1})	0.02	21.98	2.17	0.25	**24.42**
strong jet ($wind_{max} > 4$ m s^{-1})	0.00	2.30	0.07	0.00	**2.37**
no jet-weak ($wind_{below100m} < 2$ m s^{-1})	0.08	12.10	8.32	2.05	**22.55**
no jet-moderate ($wind_{below100m} \geq 2$ m s^{-1})	0.12	20.45	3.29	0.81	**24.67**
total	**0.26**	**74.91**	**20.70**	**4.13**	**100.00**

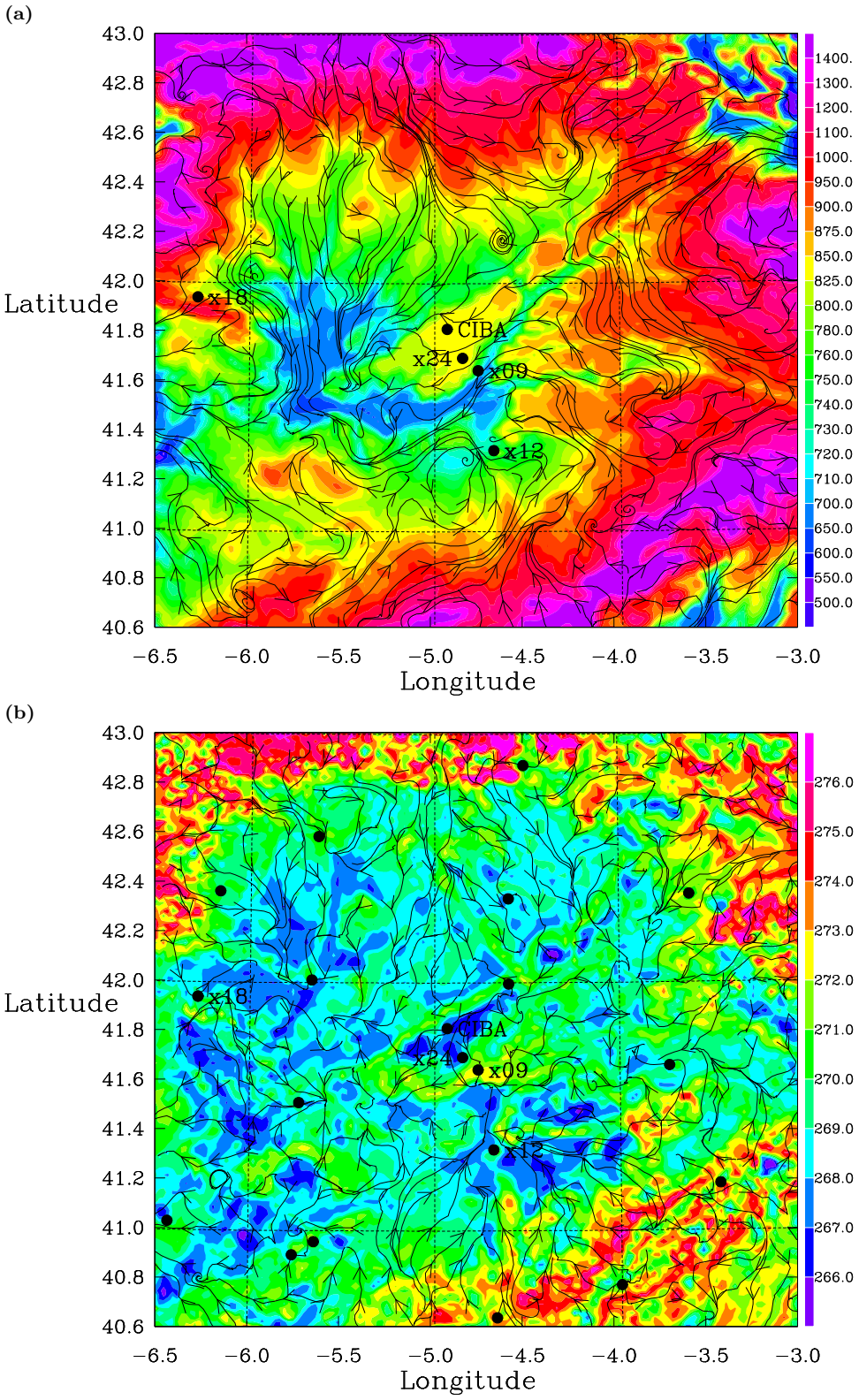

Fig. 1 (a) Topography (in m) of the centre of the Duero basin and simulated streamlines at 50 m height at 0200 UTC. The locations of 4 AWS from AEMET are displayed in dots. The 100-m tower in the CIBA site is located in the Torozos Plateau, an elevated area in the centre of the basin. (b) 1.5-m temperature (in K) and streamlines at 0200 UTC. In both plots, the streamlines are plotted every 4 gridpoints (8 km).

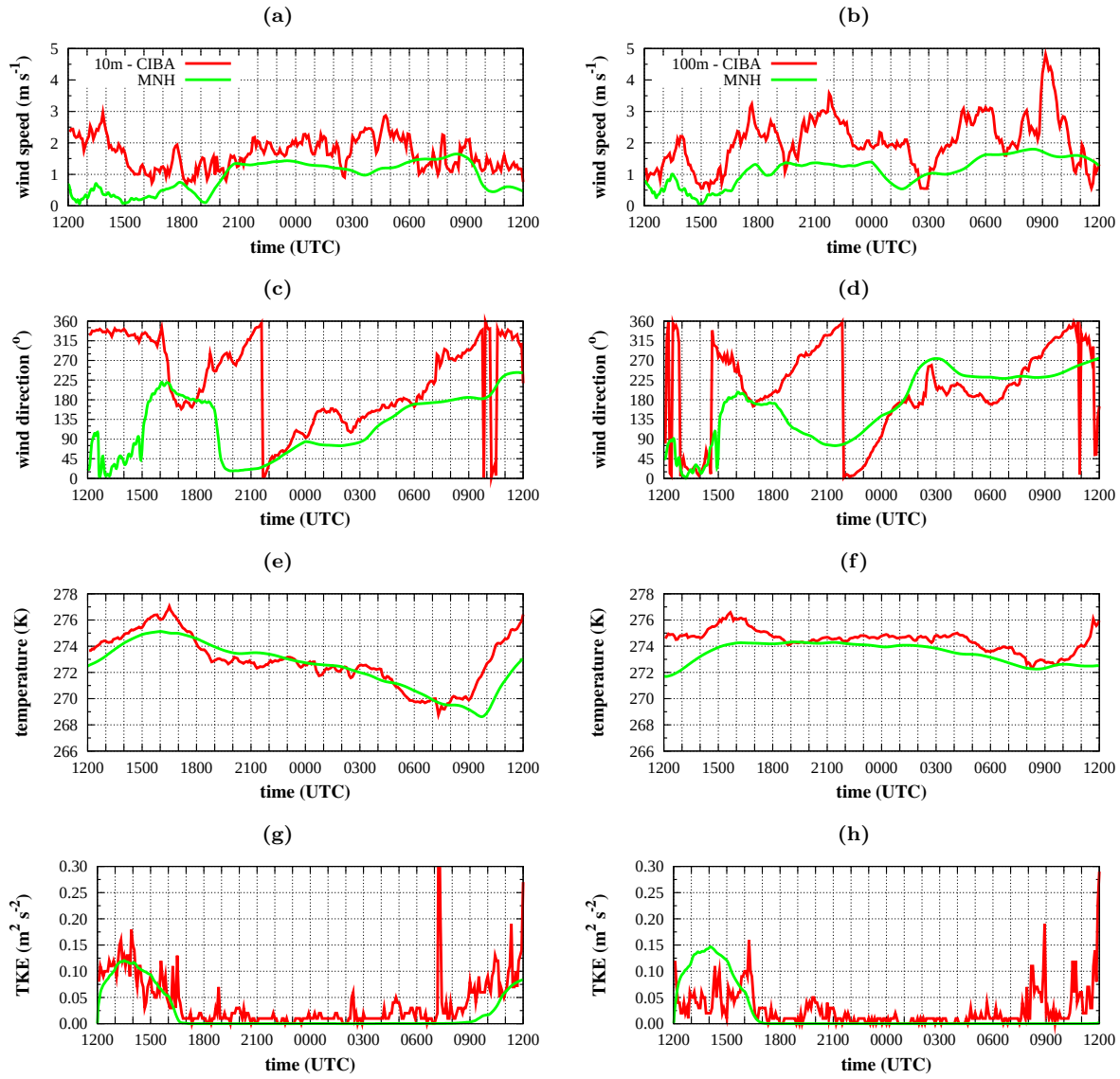

Fig. 2 Time series measured by the CIBA tower compared to those obtained from mesoscale runs for (a) and (b) wind speed, (c) and (d) wind direction, (e) and (f) temperature and (g) and (h) TKE at (left) 10 m a.g.l. and (right) 100 m a.g.l. CIBA data correspond to 5 min averages whereas the model results correspond to outputs every 1 min.

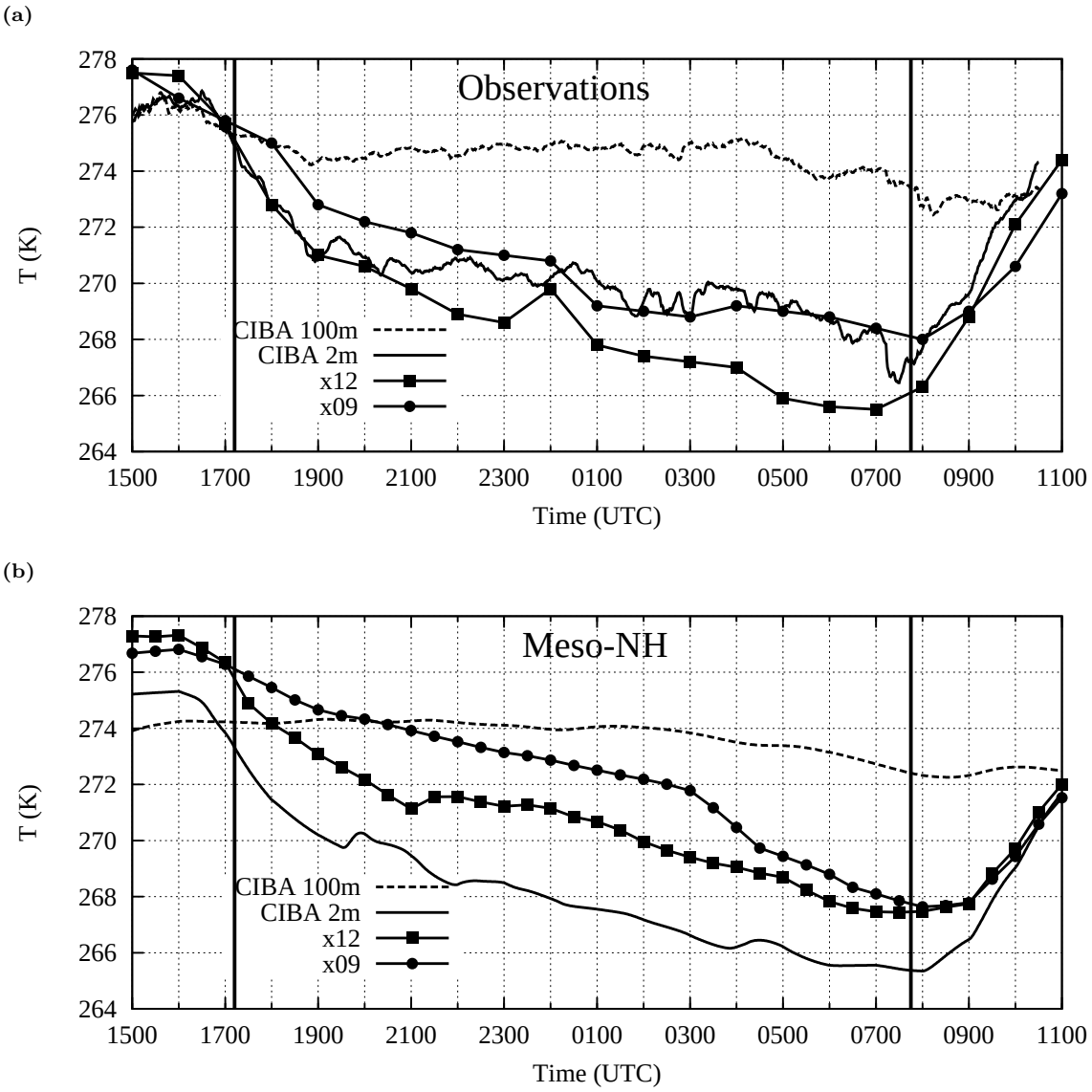

Fig. 3 Time evolution of the temperature at the top of the tower and at 1.5 m a.g.l. for Olmedo (x12), Valladolid (x09) and the CIBA site (a) measured and (b) simulated. See Figure 1 for locations. Bold vertical lines indicate the sunrise and sunset times.

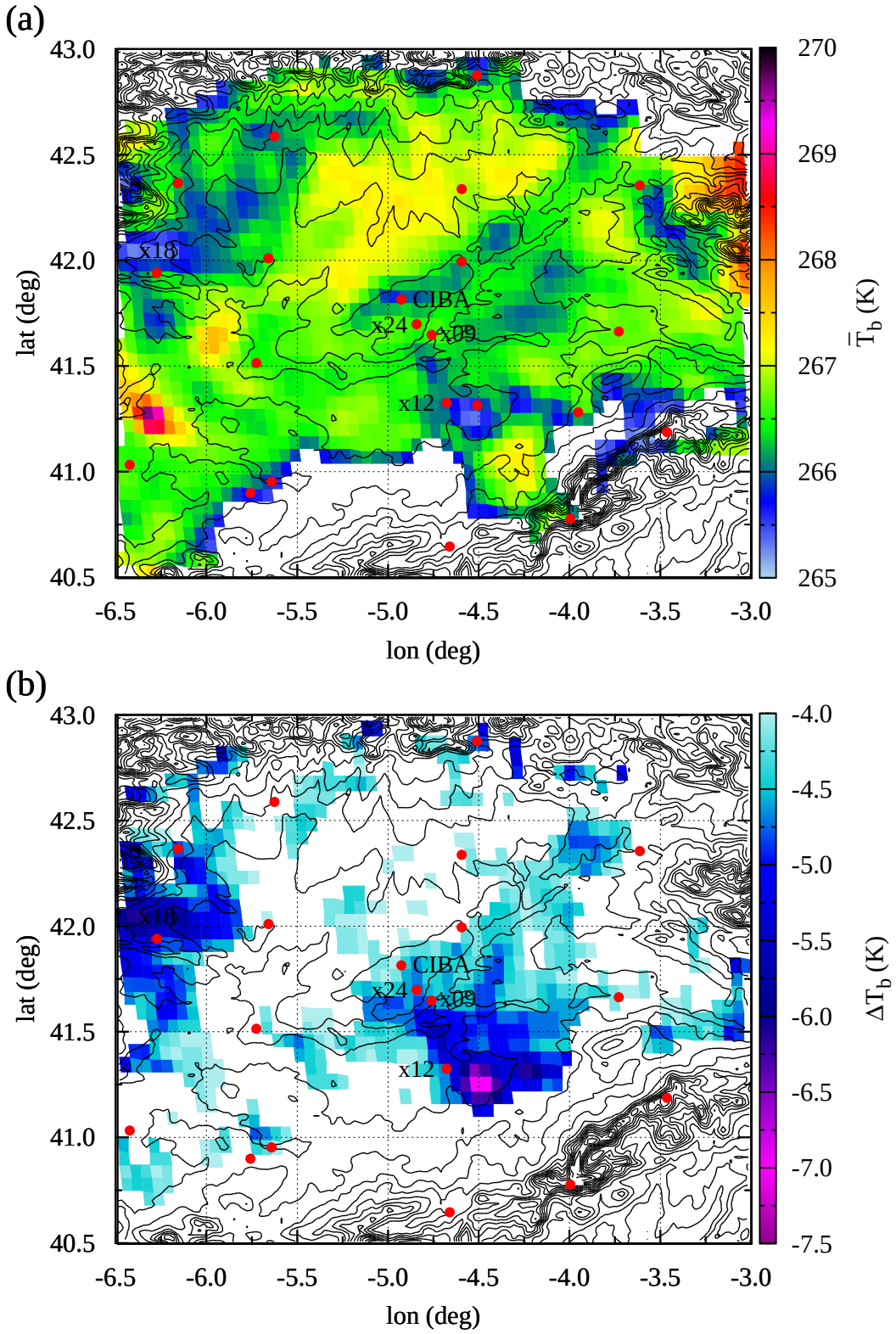

Fig. 4 (a) Mean nocturnal temperature $\overline{T}_b(\mathbf{x})$ for the Duero basin derived from Meteosat-7 (without the snow area). (b) Total cooling from the beginning of the night (1730 UTC) to just before sunrise (0730 UTC). Only points with a total cooling equal or greater than 4 K are represented. In both plots, surface elevation contours are plotted every 100 m within the range 500 - 2100 m a.s.l. The locations of the AWS from AEMET are displayed with dots.

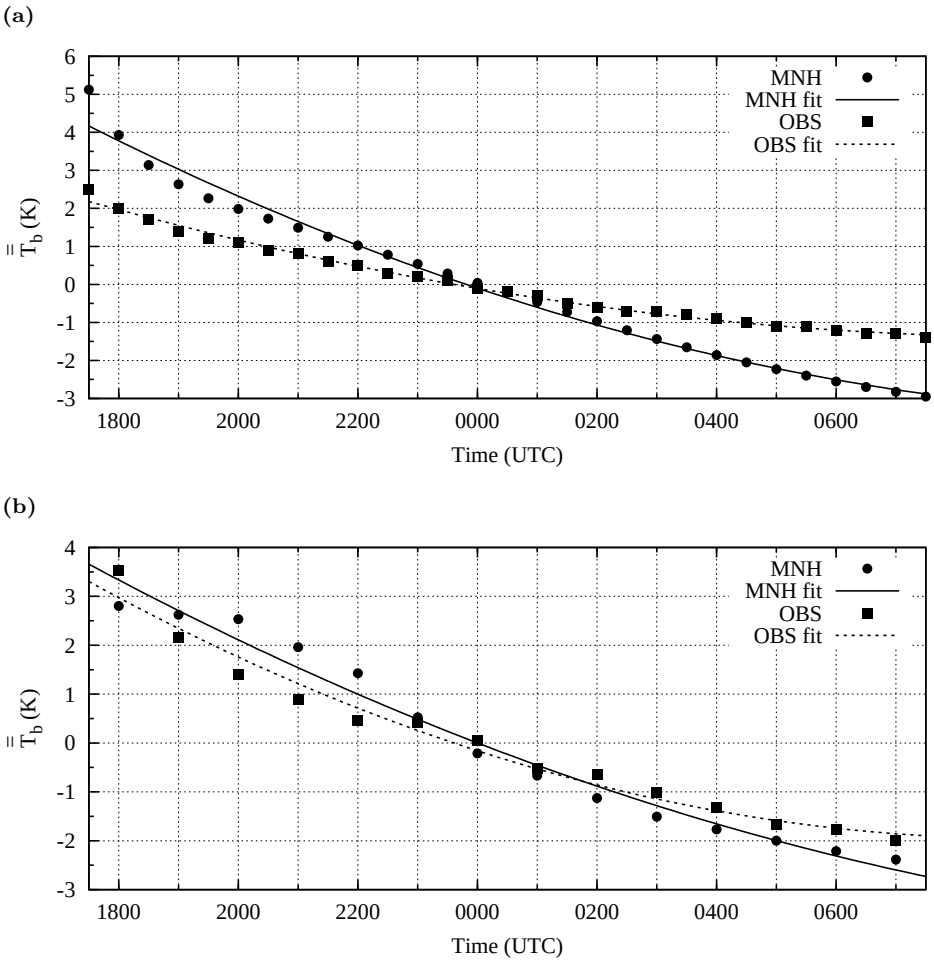

Fig. 5 (a) Basin-averaged deviation of the radiative surface temperature from the mean nocturnal temperature $\overline{\overline{T}}_b(t)$ between sunset and sunrise from the mesoscale simulation and from the satellite data. (b) The same as (a), but for the 1.5-m temperature with the observations taken from the AWS.

(a)

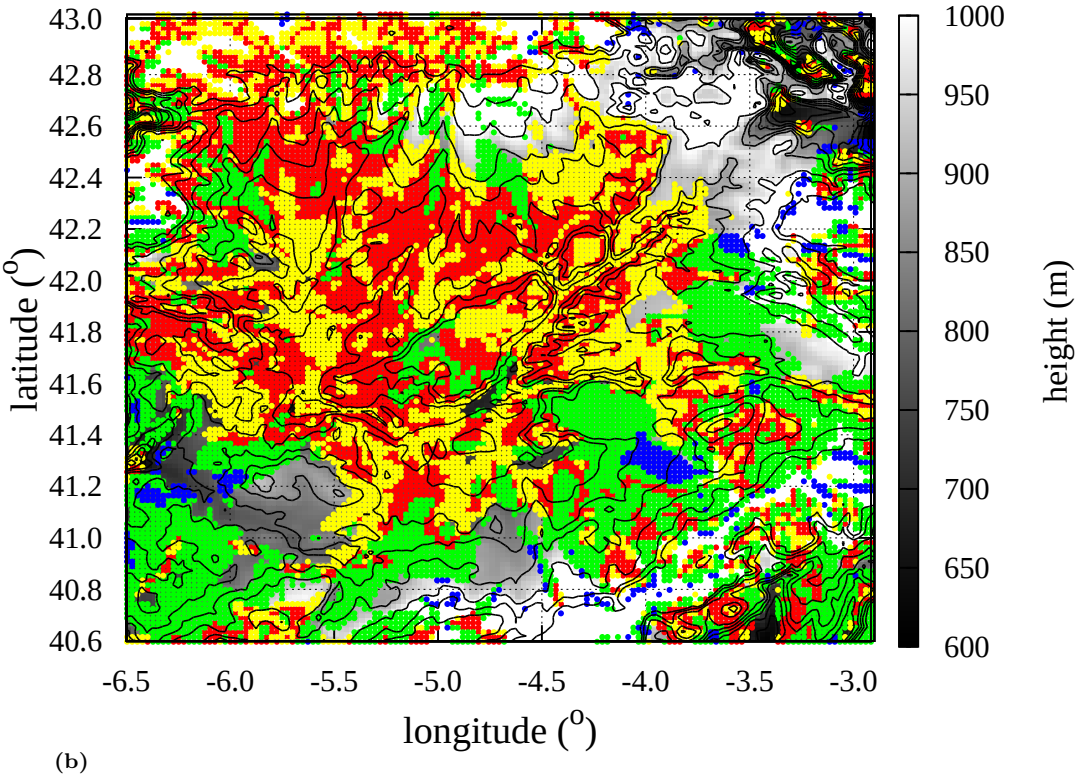

(b)

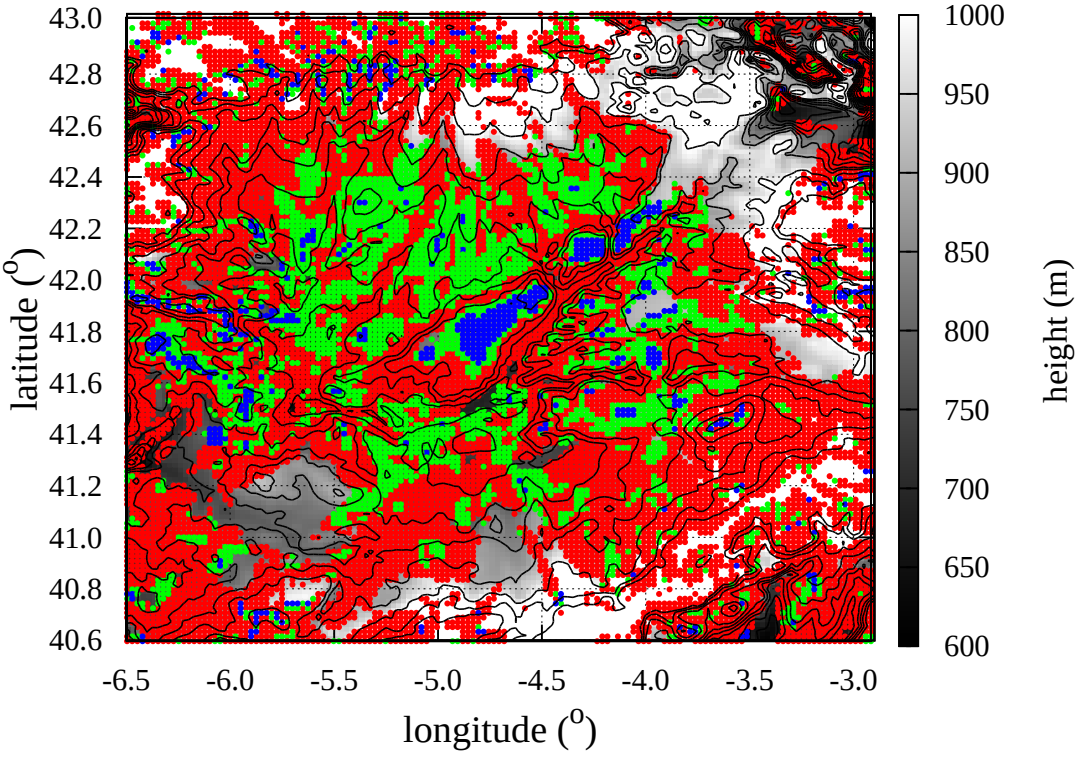

Fig. 6 Location of the points corresponding to the categories in Table 1. (a) Classification according to the wind maxima up to 100 m a.g.l.: (red) weak jet, (green) moderate jet, (blue) strong jet and (yellow) no jet (when the wind speed up to 100 m is smaller than 2 m s^{-1}). The topography is plotted in grey scale for the range of 600-1000 m a.s.l. (b) The same as in (a), but for the classification according to the strength of stratification in the surface layer: (red) weakly stratified, (green) moderately stratified and (blue) strongly stratified. In both plots, data classified as no jet-moderate in Table 1 are excluded.

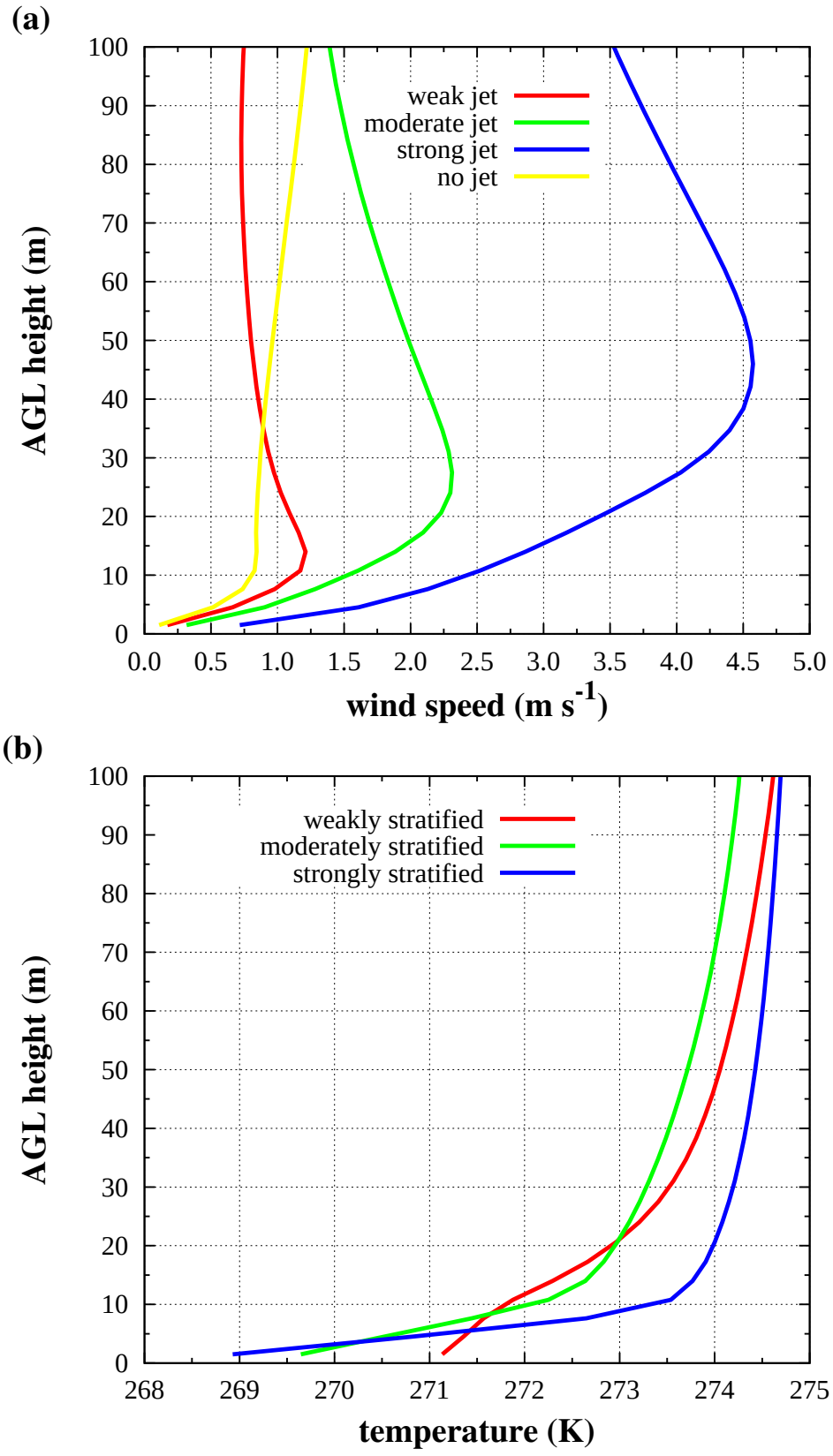

Fig. 7 (a) Averaged wind speed profiles of the classified categories according to the wind maxima classification in Table 1. (b) Averaged temperature profiles for the categories in Table 1 based on the strength of stratification in the surface layer. In both plots, data classified as no jet-moderate in Table 1 are excluded.

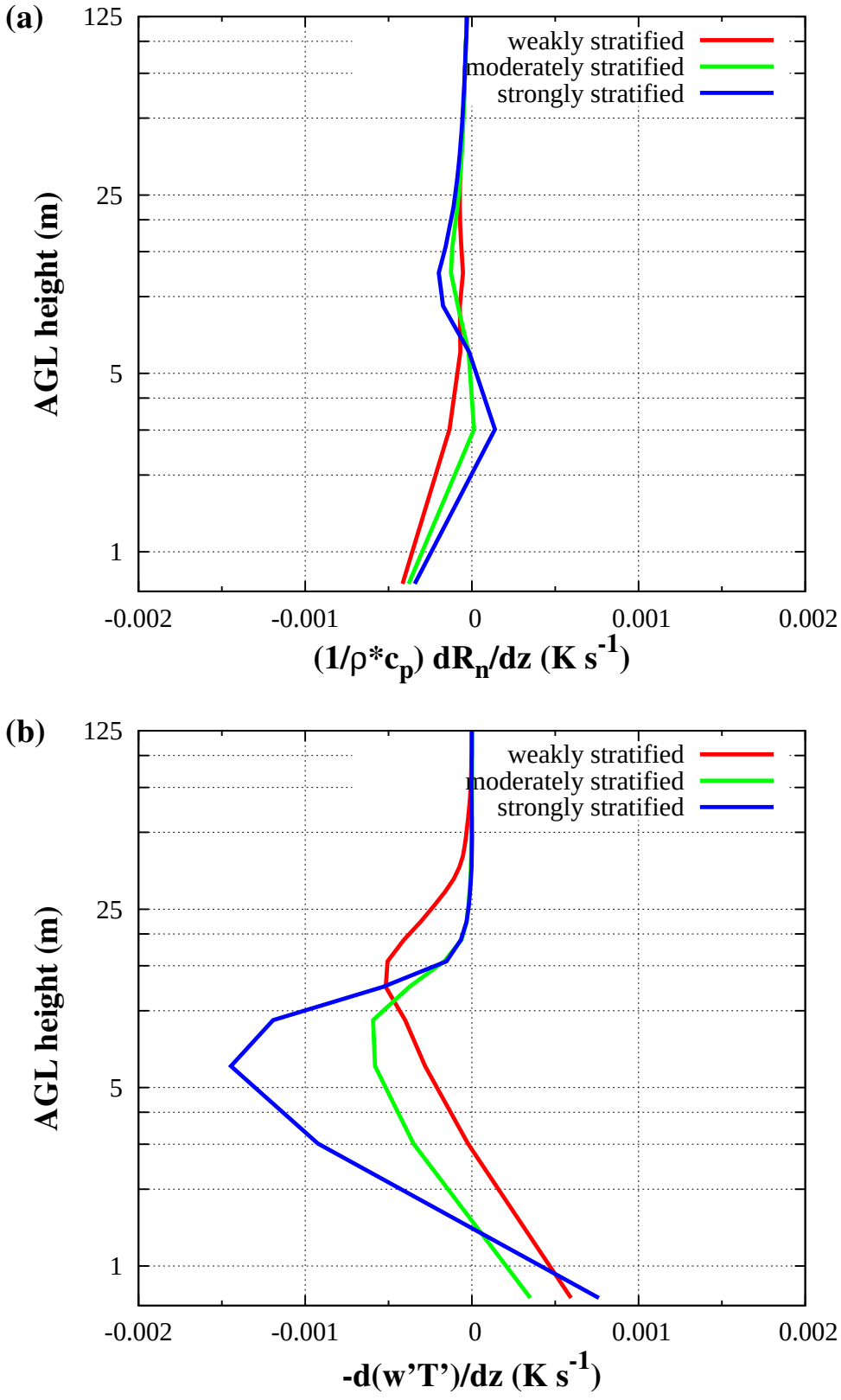

Fig. 8 Averaged profiles of (a) radiative and (b) turbulent coolings for the categories in Table 1 based on the strength of stratification in the surface layer shown in Figure 7b.